Available online at www.sciencedirect.com

ScienceDirect

Procedia Manufacturing 53 (2021) 472–483

Procedia MANUFACTURING

www.elsevier.com/locate/procedia

49th SME North American Manufacturing Research Conference, NAMRC 49, Ohio, USA

Direct Droplet Writing – A Novel Droplet-punching Capillary-splitting 3D Printing Method for Highly Viscous Materials

Yang Xu[a], Fangjie Qi[a], Xiangyun Gao[b], Yujie Shan[b], Yun Zhou[b], and Yong Chen[a,b]*

[a]*Daniel J. Epstein Department of Industrial and Systems Engineering, University of Southern California, Los Angeles, CA, 90089, USA*
[b]*Aerospace and Mechanical Engineering, University of Southern California, Los Angeles, CA, 90089, USA*

* Corresponding author. Tel.: +1-213-740-7829; fax: +1-213-740-1120. *E-mail address:* yongchen@usc.edu

Abstract

The drop-on-demand (DOD) based three-dimensional (3D) printing methods can fabricate an object with a high level of accuracy and shape complexity using multiple materials. However, a key limitation of the DOD approaches such as ink jetting is only the inks with low viscosity can be used. Such low-viscosity restriction severely limits the material options for the DOD-based 3D printing methods. To address the viscosity issue, we have developed a novel drop-on-demand 3D printing method called direct droplet writing (DDW) for highly viscous material. One main idea of the DDW process is to use direct droplet-punching to enable the printing of materials that may have a viscosity over 190,000 mPa·s; and another main idea of the DDW process is to use capillary-splitting to avoid common issues of various ink-jetting approaches, including splashing, droplet deflection, and satellite droplets. The DDW process can reliably fabricate 3D structures using a wide range of materials that are challenging for the jetting-based and extrusion-based methods. Analytical models to characterize the DDW process are presented. A set of test cases have been conducted using the in-house developed prototype system to characterize the relationship between droplet size and process parameters such as droplet punching speed and dispensing gap. Various materials, including high-loading photocurable tricalcium phosphate (TCP) ink and polyurethane (PU) leather ink, were successfully used in the DDW process. In addition to a much broader range of 3D printable materials, the DDW process is robust, without ink clogging or leaking, and can achieve consistent printing results using digitally controlled droplets.

Keywords: Additive manufacturing; Drop-on-demand; Viscous material; Multi-material; Droplet writing

1. Introduction

New methods of depositing materials will advance various applications in medical science, industry, and daily life, such as prosthesis [1, 2], electronics [3], foods [4], robotics [5-7], and batteries [8, 9]. To date, material jetting is one of the most popular technologies capable of generating and depositing controlled droplets. Fig. 1a illustrates the principle of the material jetting process. Rather than a continuous flow of liquid material, a sequence of discrete droplets on demand (DOD) is ejected out of small nozzles by micro piezo (Fig. 1a vs. Fig. 1c). The ejected droplets, after separating from the nozzles, land in places that can be precisely controlled. The deposited materials usually become solid by a solvent's evaporation or photocured by an additional ultraviolet lamp. A unique feature of this DOD approach is its capability of controlling an object's property voxel by voxel. Such ability to create "digital materials" has been demonstrated by manufacturing objects with varying colors and transparency [10, 11], metamaterials [12], and functionally graded materials [13-15]. Despite the superiority in droplet control, the material jetting process strongly suffers from low-viscosity restriction, which dramatically limits the material options. For example, only the materials with a viscosity lower than 40 mPa·s can be successfully ejected by the commercial inkjet printheads [16]. Besides, the contactless jetting mode with a certain gap between the jetting nozzles and the build platform also brings troubles. Satellite drops between primary droplets and splashing during droplet impact often occur without optimizing material surface tension and rheological properties and fine-tuning process parameters, including pulse waveform and stand-off distance [17].

On the other side, the syringe-based direct ink writing (DIW) method is a popular three-dimensional (3D) printing method that

2351-9789
10.1016/j.promfg.2021.06.050

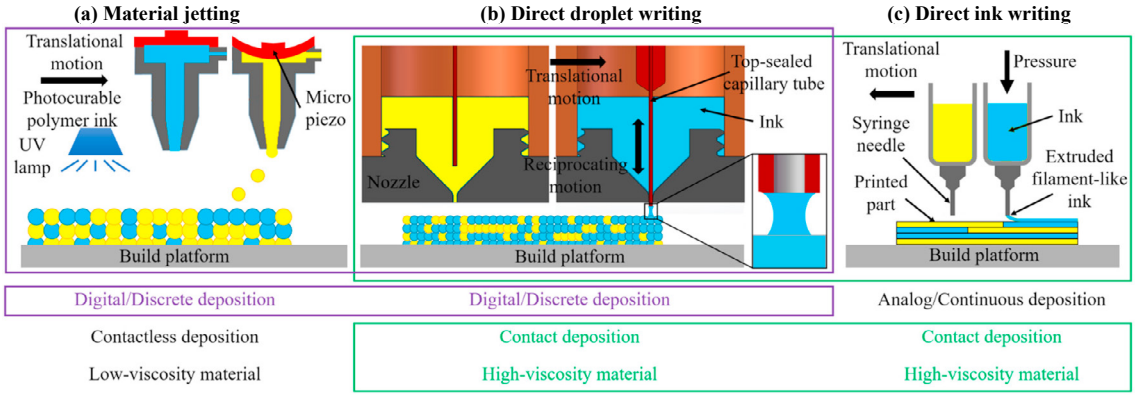

Fig. 1. Comparison of our approach (direct droplet writing) with material jetting and direct ink writing. (a) A schematic to illustrate the principle of material jetting; (b) a schematic to illustrate the principle of direct droplet writing; and (c) a schematic to illustrate the principle of direct ink writing.

enables materials over a wide range of viscosity (from 1 to over 1,000,000 mPa·s) [17]. It can fabricate patterns using various materials, including high viscosity such as highly concentrated colloidal suspensions of ceramic powders. The filament of paste-like material is extruded from a small nozzle continuously while the nozzle is moved across a build platform (See Fig. 1c). The continuous material filament keeps contact with the build platform or the previously built layers. Hence the process is more robust than contactless material jetting. Multiple nozzles can be involved in the printing process to achieve multi-material 3D printing capability. However, this continuous material deposition approach loses the ability to define an object's property voxel-by-voxel [18]. It also restricts shape complexity and limits its use in many applications such as lattice structures [19], full-color parts [11], and many others [20, 21]. Besides, highly viscous solutions used in DIW require high pressures that may damage the dispensing tip [17].

Overall, the DOD method, such as material jetting, is more promising in terms of the digital droplet control at each voxel. In contrast, the DIW method has advantages in handling viscous materials and robustness. To inherit both sides' merits, we developed a novel contact-based and digital droplet-on-demand approach for highly viscous materials in this paper. The newly developed process is called direct droplet writing (DDW). The schematic of our method is shown in Fig. 1b. Inspired by the metal sheet shearing process, such as punching and blanking, we utilize a top-sealed capillary tube to punch a tiny amount of ink from a small nozzle onto the build platform. Then the ink is deposited on the build platform or the previously built layers by capillary bridge splitting. Only one single droplet will be precisely deposited in each deposition cycle with no satellites nor droplet slashing. At the same time, the mechanical punching force is big enough to work with highly viscous materials (over 190,000 mPa·s, See Fig. 12A). The details of the DDW process are presented in Section 2.

1.1. Related works

Since the main focus of this paper is to achieve a novel DOD approach to address the material viscosity, satellite drops, and splashing issues, a summary of the related work is given first in this section, including the previous efforts to dispense viscous materials into droplets for 3D printing.

(1) To generate droplets of material with a viscosity of more than 100 mPa·s, one must rely on more powerful jetting techniques. Laser-induced forward transfer (LIFT) employs a laser beam to transfer liquid source adhering to the bottom of a transparent disk coated with a carrier material [22-24] (Fig. 2A-a). When a laser pulse strikes the coating, a fraction of the coating material decomposes into gas. The trapped gas propels liquid source material downward onto a receiver substrate (Fig. 2A-b). By increasing laser fluence, the ink of 8,278.9 mPa·s can be jetted [24]. However, the LIFT mechanism determines the receiver substrate and the donor disk need to be flat and parallel to each other. The volumetric transfer rate depends on the source material thickness, dispensing distance, laser fluence, and material property. The optimization of these parameters is challenging, especially for materials whose properties change over time in the open air. It is also relatively hard to refill source material since the donor disk needs to be prepared before printing.

(2) Instead of using laser-related energy, electrohydrodynamic jet printing uses electrical forces to deposit droplets at high speed and resolution (~50 nm) [25, 26]. The principle of the electrohydrodynamic jet printing process is shown in Fig. 2B. However, this method requires materials with specific electromagnetic properties and precise coupling between the nozzle, substrate, and the existing printed features to induce the desired electrical field [27].

(3) Various DIW methods have been developed by adding a piezo-driven valve and a heating device [28-30]. The valve-based approach can achieve droplet dispensing ability while inheriting the viscous material processing ability. With these modifications, continuous liquid flow with a viscosity of

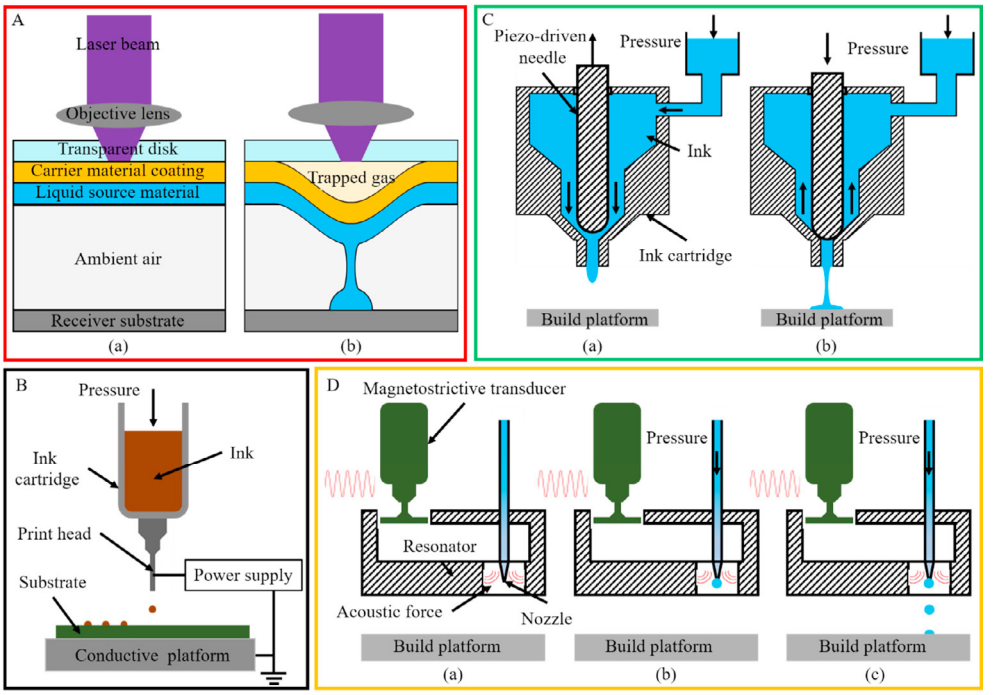

Fig. 2. A summary of some previous work. (A) Principle of laser-induced forward transfer (LIFT) (adapted from [23]). (a) A thin layer of carrier material absorbs the pulse laser energy; and (b) a portion of carrier material is ablated into a confined pocket of gas and strikes the remaining material away from the transparent disk. If the impulse energy is sufficient, a small amount of liquid source material will be transferred onto the receiver substrate. (B) Principle of electrohydrodynamic jet printing (adapted from [25, 26]). (C) Principle of the valve-based jetting method (adapted from [28-30]). (a) When the piezo-driven needle moves upward, ink flows out from the nozzle under pressure; and (b) when the piezo-driven needle moves down to its original position, the ink flow will be separated into two parts. The ink that has flowed out of the nozzle will land onto the build platform. (D) Principle of acoustophoretic printing (adapted from [27]). (a) In the normal state, the magnetostrictive transducer keeps on while no material is extruded out; (b) when dispensing droplets, the material is extruded out by pressure and forms a droplet attaching to the nozzle orifice; and (c) the acoustic force and gravitational force will increase as the droplet volume increases and finally detach droplets from the nozzle.

15,300 mPa·s can be converted into discrete droplets. This valve-based approach extrudes ink continuously as elongated filament under a constant pneumatic pressure similar to DIW (Fig. 2Ca). It utilizes a piezo-driven needle-like valve to cut off ink flow (Fig. 2Cb). The landed ligament will form a droplet on the substrate. A heating device is used to melt solid plastic and reduce material viscosity [28]. One kind of material's printability is strongly coupled with constant pneumatic pressure, material physical property, pulse shape for the piezo valve, and drop spacing. In this valve-based approach, the undesirable ligament tail and splashing phenomenon will lead to an uncontrollable pattern shape and decrease printing resolution. The ligament results from the extruded ink cannot separate from the nozzle timely and form droplets. In the dripping ink phase (Fig. 2Cb), only gravitational force $G = \rho V g$ (where ρ is ink density, V denotes droplet volume, g represents gravitational acceleration) takes effect to overcome capillary force $F = \pi \gamma D$ (where γ is ink surface tension, D is nozzle diameter).

(4) In addition to mechanical pressure, acoustic radiation force is also applied to overcome the capillary force by surrounding the nozzle orifice with a resonator driven by a transducer [27] (Fig. 2Da). With the increased dragging force (acoustic radiation force plus gravitational force), the pendant liquid filament is easier to split from the source material in the nozzle and form droplets (Fig. 2Db and 2Dc). This method can even work with highly viscous materials like honey (25,000 mPa·s). However, to apply the acoustic force, the nozzle orifice must be located within a specific height range inside the resonator, such that the acoustic wave is reinforced and can provide a desired downward force. The minimum stand-off distance is larger than the conventional material jetting methods (0.5-1 mm). A larger stand-off distance will increase the deflection of the landed droplet that decreases its positional accuracy. Moreover, the acoustic force will intensify this positional error, especially for more viscous ink that needs more powerful acoustic radiation. Since this method is similar to "natural" tap dripping, the dripping speed will decrease with the increase of material viscosity. For material with a viscosity higher than 10,000 mPa·s, the max ejection frequency is lower than 4 Hz [27].

1.2. Contributions

In this work, we present a low-cost DDW process to realize the droplet-on-command 3D printing using highly viscous materials (up to 190,000 mPa·s, Fig. 12A). It also has no adverse effects from satellite droplets, droplet splashing, and

deflection. In the DDW process, only one single droplet will be precisely deposited in each dispensing cycle at the point where the tool touches the substrate. Also, the DDW process is robust and reliable since the printing parameters, and the change of material viscosity will not affect material printability. We demonstrate the droplet size can be varied by adjusting printing parameters, including the punching speed and dispensing gap. This digital droplet-on-command method allows printing 3D complex structures on various substrates with different shapes and textures. Finally, since this work focuses on addressing the DOD's dilemma regarding material viscosity, satellite drops, and splashing issues, we present a set of test cases using highly viscous photocurable tricalcium phosphate (TCP) ink and self-solidifiable polyurethane (PU) leather ink to demonstrate the DDW method's efficacy and versatility. The printing results show that the DDW process will drastically broaden the range of 3D printable materials and significantly advance the droplet-based 3D printing method in fabricating functional structures in the future.

2. Direct droplet writing process

2.1. Droplet punching

To print materials with high viscosity, shear stress that is orders of magnitude larger than that of current methods, such as electric field, acoustic force, and valve pressure, is required. Inspired by the metal sheet shearing process, such as punching and blanking, we directly use mechanical force in the shearing direction in the DDW process so a large force can be directly applied to a small portion of highly viscous liquids to make it more flowable. Due to the smaller area for a large punching force and the well-known shear-thinning phenomenon (See Fig. 12Ag), our method based on droplet punching can handle the printing materials with a viscosity at 190,000 mPa·s (See Fig. 12A).

Each cycle of our dispensing approach involves two main stages. In the first stage, as shown in Fig. 3A, a top-sealed capillary tube is driven by a mechanical force to split a tiny amount of ink from the ink stored in the cartridge. The capillary tube working as a hollow "puncher" moves downward at a constant speed v and passes through the opening nozzle (Fig. 3Ab). Therefore, the capillary tube and the nozzle hole are clearance fit. During this process, a small fraction of ink rushes in the capillary tube and is captured by the tube channel because of surface tension and the pressure rise induced by the tube movement, while most of the ink blocking the tube is pushed away (See Fig. 3Ab). The following force balance governs the volume of the trapped ink inside the tube.

$$F_{ct} + F_t = F_a + G_t \tag{1}$$

Where the force resulting from a capillary rise $F_{ct} = \pi d_t \gamma \cos\theta_{ct}$, where d_t is the inner diameter (ID) of the tube; θ_{ct} is the contact angle between ink and tube surface; and γ is the ink surface tension. The pressure force $F_t = 0.25\pi {d_t}^2(\rho g h_t + 0.5\rho v_p^2)$, including static pressure $\rho g h_t$ and dynamic pressure $0.5\rho v_p^2$ applied on the trapped ink surface $0.25\pi {d_t}^2$, where ρ is ink density; h_t is tube length immersed in ink; and v_p is punching velocity. F_t monotonically increases with increased tube depth h_t and punching velocity v_p. The two forces (F_{ct} and F_t) are balanced by compressed air pressure force F_a and corresponding gravitational force G_t. $F_a = \frac{P_0 V_0}{4(V_0 - V_t)}\pi d_t^2$, where P_0 is the standard atmospheric pressure; V_0 is the internal volume of the capillary tube; and V_t is the volume of ink trapped inside the capillary tube. $G_t = \rho V_t g$, where g is the gravitational acceleration.

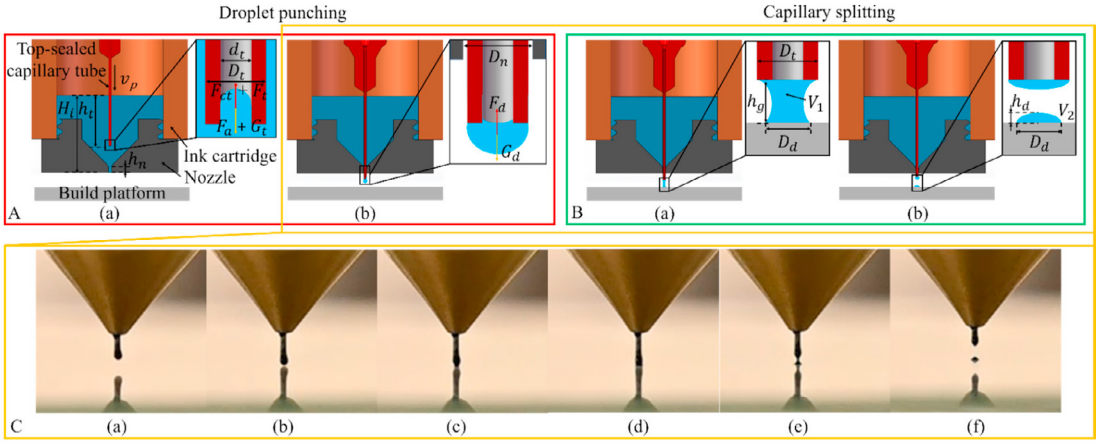

Fig. 3. Mechanism of direct droplet writing. (A) Schematic diagram of the first stage of DDW– droplet punching. (a) A tiny amount of ink captured by the capillary tube moving downward; and (b) the punched-out ink droplet hanging on the capillary tube tip. (B) Schematic diagram of the second stage of DDW– capillary splitting. (a) Liquid bridge formation; and (b) splitting of liquid bridge. (C) Photographs showing the second stage of DDW. (a) (b) The capillary tube with extruded ink droplet continues moving downward and approaches the build platform; (c) (d) a capillary bridge forms between the build platform and the tube end once the pendant ink contacts with the build platform; and (e) (f) the capillary bridge undergoes thinning and breakage, leaving a portion of ink on the build platform during the retraction of the capillary tube.

Though the ink cartridge is not sealed, the ink will not leak from the nozzle opening during the capillary tube's upward movement due to the liquid's surface tension. The volume trapped inside the nozzle orifice is:

$$V_n = 0.25\pi D_n^2 h_n \quad (2)$$

The extruded ink droplet volume is the sum of two parts – the ink trapped inside the capillary tube V_t characterized by Eq. 1 and the ink residing in the nozzle opening $V_n' = 0.25\pi D_t^2 h_n$ (around 125.6 nL).

$$V_1 = V_t + V_n' \quad (3)$$

The extruded droplet volume V_1 in the stage of droplet punching will increase as punch velocity v increases, as shown in Fig. 6a and 6b. The ejected ink droplet attaches to the bottom of the capillary tube since the maximal capillary force F_d is much larger than the gravitational force G_d (See Fig. 3Ab).

2.2. Capillary splitting

In the second stage of the DDW process, the capillary tube continues moving downward and approaches the build platform (See Fig. 3Ca and 3Cb). When the pendant ink touches the build platform, a liquid bridge will form between the build platform and the tube end, as shown in Fig. 3Cc. When the tube arrives at the lowest position (h_g higher than the build platform), the contact area between the droplet and the build platform reaches its maximum value $0.25\pi D_d^2$ (See Fig. 3Cd and Fig. 3Ba). When the capillary tube retracts from the build platform, the capillary bridge will undergo thinning and finally breakage, leaving a portion of ink on the build platform (See Fig. 3Ce and 3Cf and Fig. 3Bb). This stage is a liquid transfer process in the dynamic regime. In this case, the droplet contact diameter with both the donor surface (capillary tube in our case) and the receiver surface (i.e., the build platform or the previously built layers) will be pinned during almost the entire liquid transfer process [31].

We found that the dispensing gap h_g, i.e., the distance between the lowest tube bottom position and the substrate, will affect the deposited droplet diameter D_d and further affect the splitting ratio r, given the wettability of both contact surfaces (See Fig. 8). Therefore, the deposited ink volume on the substrate in the second stage V_2 can be expressed as

$$V_2 = V_1 \times r(h_g) \quad (4)$$

Accordingly, we can use a single nozzle to dispense viscous liquid into droplets with varying droplet sizes based on these mechanisms. The detailed hardware design to realize the DDW process is discussed in Section 3. The study of crucial printing parameters such as punching speed and dispensing gap to understand the process's principle is presented in Section 4.

3. Direct droplet writing experimental setup design and analysis

3.1. Experimental setup design

To realize the accurate dispensing of viscous material into droplets at right positions, we designed a printhead based on the DDW process and build a prototype 3D printing system. We designed the printhead as an assembly of several separate parts to demonstrate the main functions required by DDW. The detailed structure is shown in Fig. 4. Various variations based on the same DDW principle can be designed for better performance and improved manufacturability in the future.

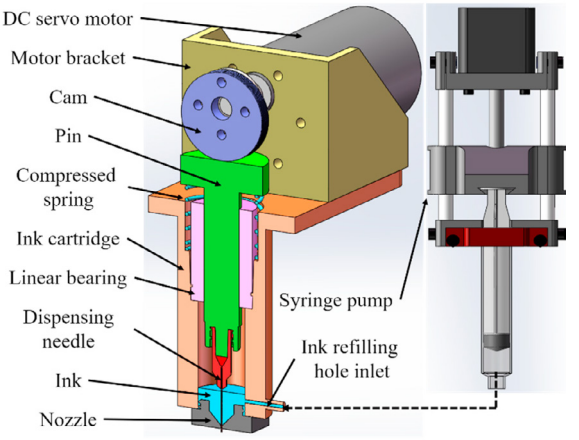

Fig. 4. DDW Printhead design.

The capillary tube that we selected is a 27 Gauge stainless steel blunt dispensing needle with a male Luer lock connector (ID = 200 μm , outside diameter (OD) = 400 μm) bought from McMaster-Carr. The needle length is 0.5 in (12.7 mm). The dispensing needle is connected to a pin with a female Luer lock connector fabricated by an SLA 3D Printer (Anycubic Photon). A cam-spring mechanism drives the combination of the pin and the dispensing needle. The cam is 3D printed via a FFF 3D printer (3DWOX1, Sindoh Corp.) and coated by XTC-3D™ (Smooth-On, Inc.) to increase its surface smoothness, impact, and abrasion resistance. 3-IN-ONE multi-purpose oil (bought from True Value) is also applied to lubricate the pin top and the cam surface. A DC motor integrated with a hall sensor controls the cam's rotation. The maximum speed of the cam is 1,000 RPM. The resolution of the sensor is 640 counts per round. The pin keeps making sinusoidal reciprocating motion vertically under the linear bearing restriction. The linear bearing is retained in the ink cartridge (fabricated by FFF) by a light press fit and a clamp ring structure. The nozzle contains a 45-degree slope followed by a round corner and a ~1 mm long channel (See Fig. 3A(a), $h_n = 1$ mm). The nozzle orifice's inner diameter is around 500 μm , which is in clearance fit with the dispensing needle. The cartridge is not sealed in our design, so the volume change inside the cartridge chamber caused by the pin movement will not affect the air pressure and the punching process.

Ink is held in the cartridge and will not leak from the bottom nozzle opening due to its surface tension. A self-built syringe (10 mL, ID = 14.5 mm) pump driven by a stepper motor is utilized to refill ink from the side inlet, which has a hole of 2 mm in diameter. The motor speed is set to 0.01 mm/s, so the torque required to push viscous material is as small as possible. The ink surface level in our setup is maintained at ~20 mm.

During the actual operation, the ink refilling is conducted recursively after depositing 500 droplets. We calculated the refilling volume by measuring the mass of 500 droplets and dividing it by its density. Take the PU leather ink shown in Fig. 12 as an example. The ink density is 1.05 g/mL. The mass of 500 PU droplets is measured as $0.010^{+0.001}_{-0.001}$ g. The measurement is repeated five times. Given the cartridge inner diameter (16 mm), we can estimate the maximum variance of the ink surface level in our case is $47\ \mu m\ (=\frac{0.01\times10^3\times10^3}{1.05\times16^2\times0.25\times\pi})$, which is only 0.235% of the original ink height (20 mm). With the cartridge connected to the open-air, combining the 2-mm wide inlet and 0.01 mm/s refilling motor speed, the pressure caused by ink refilling will not affect the printing process. The experimental study also verifies good repeatability of droplet size (See Section 4).

The printhead is mounted on a 3-axis motion system. The printhead moves horizontally above the build platform, depositing droplets of material onto the surface where material deposition is required. After dispensing materials for one layer, the whole layer can be cured by raising temperature if the material is thermally cured or by UV light if the material is photocurable. Then the build platform moves downward by the layer thickness vertically after each new layer is fabricated. An absolute indicator (iGaging, 35-700-25, San Clemente, CA) was applied to ensure the printhead was parallel to the build platform. The resolution of the indicator was 1 μm. The height variances between multiple printheads were compensated by moving the build platform in the Z axis based on their calibrated heights. The resolution of the motion system used in our prototype was 2 μm.

3.2. Self-alignment mechanism of the dispensing needle

The designed printhead for the lab demonstration was assembled from several off-the-shelf components using self-fabricated fixing components. Even with limited manufacturing and mounting accuracy, the short and thin stainless-steel dispensing needle can pass through the small nozzle with the help of the linear bearing and the internal slop of the nozzle. The self-alignment mechanism between the dispensing needle and the nozzle is analyzed as follows.

Suppose the pin moves down at a maximum speed of 1000 RPM (16.7 Hz) (See Fig. 5a). The stroke s is 5 mm. The full punching speed of the needle is $v_p = 0.167$ m/s. Suppose our manufacturing and assembling tolerance's misalignment (i.e., the distance δ between the needle and the nozzle orifice) is larger than 100 μm (Fig. 5b). Hence the dispensing needle will contact the 45-degree nozzle slope. The mechanical properties and geometric parameters of the dispensing needle used in our prototype system are listed in Tables 1 and 2.

When impacting the nozzle slope, the dispensing needle will gain a horizontal speed $v_h = v_p$ and the max deflection Δ_{max}. The impact force F applied to the dispensing tip can be calculated by Equation (5).

$$\frac{F^2 l^3}{6EI} + \frac{1}{2} m v_h^2 = F\Delta_{max} = \frac{F^2 l^3}{3EI} \tag{5}$$

Table 1. Mechanical properties of 304 stainless steel dispensing needle.

Mechanical properties	Value	Unit
Young's modulus E	1.9×10^{11}	Pa
Moment of inertia I	1.1775×10^{-15}	m^4
Section modulus W	5.8875×10^{-12}	m^3
Shear strength $[\tau]$	5.17×10^{8}	Pa
Yield tensile strength $[\sigma_Y]$	2.15×10^{8}	Pa

Table 2. Profiles of 304 stainless steel dispensing needle.

Profile properties	Value	Unit
Needle length, l	12.7×10^{-3}	m
Inner diameter, d_t	0.2×10^{-3}	m
Outer diameter, D_t	0.4×10^{-3}	m
Cross-section area, A	9.42×10^{-8}	m^2
Mass, m	0.02×10^{-3}	Kg

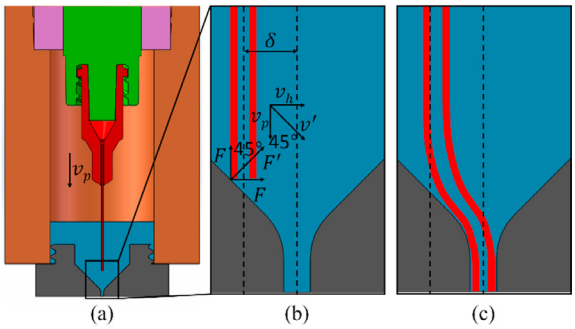

Fig. 5. Illustration of the self-alignment mechanism. (a) The dispensing needle moves down at full speed v_p; (b) the downward dispensing needle impacts with the nozzle slop; and (c) the dispensing needle is led into the nozzle opening hole through self-alignment.

Therefore, the impact force $F = 0.014$N. The impact force is far less than the buckling force limit, which is

$$F_{cr} = \frac{\pi^2 EI}{(2l)^2} = 3.42\text{N} \tag{6}$$

The maximum normal stress caused by the impact is

$$\sigma_{max} = \frac{Fl}{W} = 3.02\times10^7\ \text{Pa} < [\sigma_Y] \tag{7}$$

The maximum shear stress caused by the impact is

$$\tau_{max} = \frac{4F}{3A}\left(\frac{r_t^2 + R_t r_t + R_t^2}{r_t^2 + R_t^2}\right) = 2.77\times10^5\ \text{Pa} < [\tau] \tag{8}$$

Both stresses are much smaller than the material's stress limits - shear strength 5.17×10^8 Pa and yield strength 2.15×10^8 Pa. The maximum deflection Δ_{max} is tiny at 41.26 μm. Therefore, the dispensing needle will bend itself and slip along the nozzle slop. Finally, it will enter the nozzle opening hole during the downward movement (See Fig. 5c). The analysis results were also verified in our experimental results, which will be discussed in Section 4.

4. Experimental study and analysis

The process parameters of the DDW process, including punching speed v, dispensing gap h_g, and material viscosity μ, may affect the printing performance, including resolution (droplet size) and accuracy (positional error). To study their relationship, we designed test cases 1-3 for different punching speeds, dispensing gaps, and material viscosity, respectively. Based on them, we performed test cases 4 and 5 for 2D patterns and 3D structures, respectively, to demonstrate 2D/3D printing capability and, more importantly, how to calibrate process parameters for other dispensing materials. A video of the test cases can be found [32]. The performed test cases are discussed in detail as follows.

4.1. Test case 1 – Different punching speed

We fabricated rows of ink dots on a glass slide using the DDW method to study the effect of punching speed on droplet size and positional error. The dispensing gap was fixed, while the punching speed, namely the motor rotation speed, was varied. The parameter settings are listed in Table 3. The motor rotation speed was converted into dispensing needle's average punching speed by $v_p = \frac{sv_m}{30}$ and listed in Table 3. There were four parameter settings in total, and each experiment was repeated ten times. In each experiment, ten droplets were generated. The ink used in Test case 1 was photocurable resin (SI500, EnvisionTEC) mixed with 40 wt % tricalcium phosphate (TCP) powder whose average particle size is around 4 μm (purchased from Sigma-Aldrich). The viscosity of the TCP and resin slurry is shown in Table 3 and Fig. 9b.

Table 3. Parameter settings for test cases 1-3.

	Test case 1 (different punching speed)	Test case 2 (different dispensing gap)	Test case 3 (different material viscosity)
Stroke s (mm)	5	5	5
Dispensing gap h_g (μm)	180	100, 180, 220	220
Motor rotation speed v_m (RPM)	240, 480, 720, 960	960	960
Calculated punching speed v_p (mm/s)	40, 80, 120, 160	160	160
TCP concentration c (wt%)	40	40	20, 30, 35, 40
Measured viscosity μ (mPa · s)	58004	58004	1871, 6237, 22765, 58004

Table 4. Parameter settings for test cases 4-5.

	Test case 4 (line)	Test case 4 (surface)	Test case 5 (multi-layer structure)
Stroke s (mm)	5	5	5
Motor rotation speed v_m (RPM)	960	960	960
Calculated punching speed v_p (mm/s)	160	160	160
Dispensing gap h_g (μm)	180	180	180
Corresponding droplet size D_d (μm)	398.8	398.8	398.8
X/Y-axis motion speed f (mm/s)	3.8, 4.0, 4.2	4.0	4.0
Calculated droplet spacing w_d (μm)	253, 267, 280	267	267
Corresponding line width w_l (μm)		350	350
Tool path spacing w_t (mm)		0.3, 0.35, 0.4	0.3
Square length for each layer a (mm)			30, 25, 20, 15, 10, 5
Square frustum height in number of layers n			1, 2, 3, 4, 5, 6

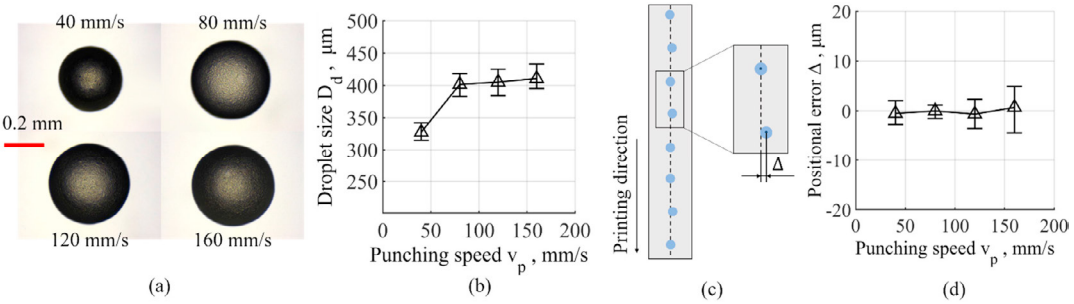

Fig. 6. Effect of punching speed v_p on droplet size D_d and positional error Δ. (a) Photographs of fabrication result using different punching speeds; (b) plot of droplet size D_d over the range of varying punching speeds v_p; (c) schematic view of droplet deposition (top) illustrating deflection errors along the printing direction Δ; and (d) plot of positional errors Δ of droplets deposited with different punching speeds v_p.

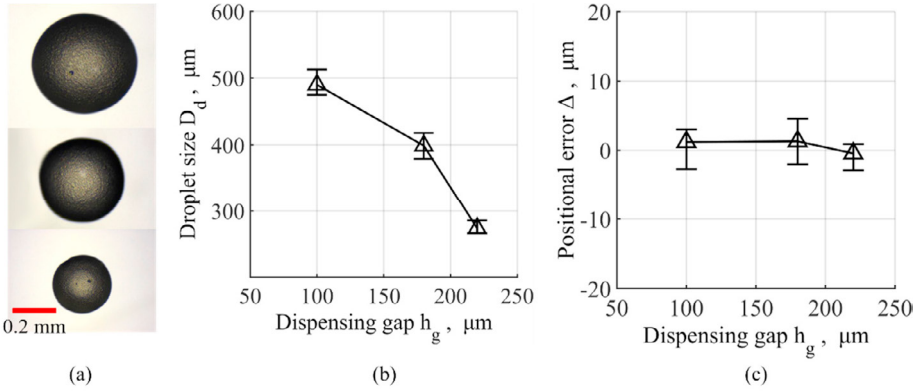

Fig. 7. Effect of dispensing gap h_g on droplet size D_d and positional error Δ. (a) Photographs of fabrication result using different dispensing gaps; (b) plot of droplet size D_d over the range of varying dispensing gap h_g explored; and (c) plot of positional errors Δ of droplets deposited at various dispensing gaps h_g.

The deposited ink dots for different punching speeds are shown in Fig. 6a. The corresponding droplet sizes are summarized in Table 5 and plotted in Fig. 6b. The droplet deposition process is illustrated in Fig. 6c. From Fig. 6b, it can be observed that the increase of punching speed from 40 mm/s to 160 mm/s leads to droplets with larger diameter sizes. This is because more ink is trapped inside the capillary tube and punched out in stage one, as shown in Eq. 1. However, when the punching speed is faster than 80 mm/s , the droplet size stabilizes and reaches a constant value. This is due to the compressed air pressure inside the top-sealed capillary tube grows faster than the dynamic pressure caused by the punching movement, and ultimately both pressures reach an equilibrium. The droplet size variation is within 5%, which shows good repeatability of the DDW process.

Table 5. Test results of droplet size under different punching speeds.

Punching speed v_p **(** mm/s **)**	**Droplet size** D_d **(** μm **)**
40	$327.6^{+14.4}_{-12.6}$
80	$401.5^{+16.5}_{-18.5}$
120	$405.1^{+19.9}_{-17.1}$
160	$410.6^{+18.4}_{-15.6}$

Positional accuracy is crucial in printing delicate structures. The positional error Δ is characterized by the deflection distance perpendicular to the printing direction (See Fig. 6c). From Fig. 6d, the average positional error is almost zero. Unlike other droplet dispensing approaches, the positional accuracy is not sensitive to dispensing speed in our method. The high positional accuracy is attributed to the contact-based process and the small dispensing gap.

4.2. Test case 2 – Different dispensing gap

Following the same procedure described in Test case 1, rows of ink dots were fabricated on the glass slide to study the effect of dispensing gap size on droplet size and positional accuracy. The motor speed was fixed at 960 RPM considering printing efficiency. The corresponding punching speed was 160 mm/s **.** The dispensing gap was varied. The ink for Test case 2 is the same photocurable slurry that was used in Test case 1. The parameter settings are listed in Table 3. If the dispensing gap reaches above 0.24 mm, the punched-out droplet cannot touch the build platform. No ink droplet will be deposited on the build platform, and all the punched-out inks will be returned to the cartridge. Therefore, we set the maximum dispensing gap at 0.22 mm in the test.

The test results regarding the dispensing gap effect on the droplet size and positional error are listed in Table 6 and shown with a diagram in Fig. 7.

Table 6. Test results of droplet size at various dispensing gaps.

Dispensing gap h_g **(** μm **)**	**Droplet size** D_d **(** μm **)**
100	490.0^{+23}_{-15}
180	$398.8^{+19.1}_{-19.8}$
220	$273.9^{+12.1}_{-6.9}$

As shown in Fig. 7a and 7b, enlarging the dispensing gap h_g will lead to a smaller droplet diameter D_d . This is because, according to [31], the transfer ratio in the dynamic liquid transfer process is dominated by the droplet contact diameter D_c on both surfaces (See Fig. 8a). Besides, the contact diameter D_c will be pinned during the entire liquid transfer process. By controlling the dispensing gap h_g , we can achieve different contact lines between the droplet and the substrate and further change the droplet diameter D_d since they are positively correlated, as shown in Fig. 8a.

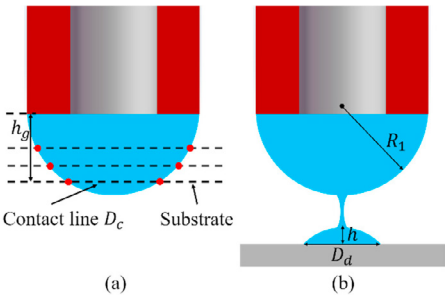

Fig. 8. (a) Schematic diagram on the influence of the dispensing gap and the contact line with a substrate; and (b) schematic diagram of droplet splitting.

The capillary pressure inside the deposited droplet and the residual droplet at the receding end are equal (See Fig. 8b). Taking the Laplace Equation into account [33], the relationship is represented as

$$\frac{2h}{(D_d/2)^2+h^2}=\frac{1}{R_1} \tag{9}$$

In this way, the transfer ratio $r(h_g)$ can be varied to get different droplet volumes, as shown in Eq. 4.

The maximum droplet size variation is about 5%, which shows our approach's good printing repeatability. For the positional error, similar behavior as Test case 1 can be observed from Fig. 7c. The average positional error is almost zero. Unlike the other droplet dispensing methods discussed in Section 1.1, the DDW's positional accuracy is not sensitive to the dispensing gap. The high positional accuracy is attributed to the contact-based droplet splitting process.

4.3. Test case 3 – Different material viscosity

Material viscosity plays a significant role in determining material printability in the aforementioned droplet-based approaches discussed in Section 1.1. Thus, for a given punching speed and dispensing gap, materials with various viscosities were used for the DDW-based droplet deposition to explore the influence of ink viscosity. The material viscosity was varied by mixing photocurable resin with TCP powders using different mass ratios. The parameter settings and the measured viscosity of the mixed slurry for each mass ratio are given in Table 3.

As shown in Fig. 9, for the slurry with a broad range of viscosity (1,800 ~ 58,000 mPa·s), the effect of material viscosity on the deposited droplet size is negligible given the same process parameters. This behavior is consistent with the model presented in Section 2 to describe the depositing process because the material viscosity does not appear in the model. The minor variations of the droplet sizes come only from the difference in ink density and surface tension. The DDW method's insensitivity to material viscosity brings another advantage compared with other DOD and DIW methods, such as the valve-based and laser-induced jetting approaches. Consequently, we do not need to adjust printing parameters frequently to make materials jettable to accommodate the potential viscosity changes due to the changing temperature or the evaporation of the solvent in ink. In comparison, such adjustments are required for most DOD and DIW methods.

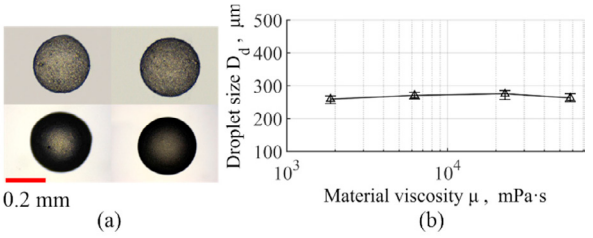

Fig. 9. Relationship between droplet size D_d and material viscosity μ. (a) Photographs of fabrication result using inks of different viscosity; and (b) plot of droplet size D_d with varying material viscosity μ.

4.4. Test case 4 – Fabrication of 2D patterns

After studying the deposition of individual droplets using the DDW process, we tested the printing of lines and surfaces to find the suitable *XY*-axis motion speed and the line spacing in the tool paths to generate continuous features that are as smooth as possible. The punching speed and the dispensing gap were fixed in the study, so the droplet size remained unchanged. The ink for the test case was the same as Test case 1. The parameter settings for the line printing are listed in Table 4.

Ideally, the *XY* linear stage's motion speed should coordinate with the droplet punching speed to get a continuous and smooth line, as shown in Fig. 10Aa and 10Ad. Otherwise, an unconnected or rugged line will be produced when the stage motion speed is faster than the droplet generation speed (Fig. 10Ac). In contrast, a thicker line will be generated if the stage motion speed is slower than the droplet punching speed (Fig. 10Ab). An interesting phenomenon is the fabricated line width w_l (~350 μm) is smaller than the droplet size D_d (~400 μm). This is because the droplet is stretched by the pin's horizontal movement during the contact period, leading to a slightly thinner line.

Following the same logic, the tool path spacing in printing a surface is also essential to ensure no internal gaps (See Fig. 10Ba). The parameter settings for the surface test are listed in Table 4. Overly large spacing will result in inner holes or gaps (See Fig. 10 Bb and 10Bc).

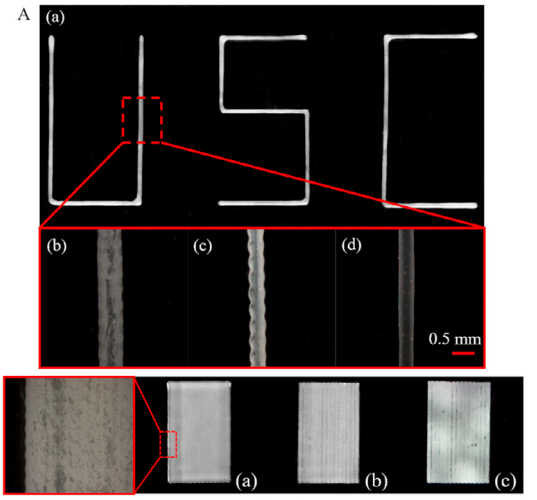

Fig. 10. Study on 2D pattern printing. (A) Photographs of lines printed using different motion speeds. (a) Lines printed with motion speed 4.0 mm/s; (b) microscopic image of the line printed with motion speed 3.8 mm/s; (c) microscopic image of the line printed with motion speed 4.2 mm/s; and (d) microscopic image of the line printed with motion speed 4.0 mm/s. (B) Photographs of surfaces printed using different tool path spacing. (a) Surface printed with tool path spacing 0.3 mm; (b) surface printed with tool path spacing 0.35 mm; and (c) surface printed with tool path spacing 0.4 mm.

4.5. Test case 5 – Fabrication of multi-layer structure

To study the layer thickness, we printed a square frustum with six layers and measured its height. The ink for the test case

is the same as Test case 1. The corresponding parameter settings are listed in Table 4. The CAD model shown in Fig. 11a was used for the layer thickness testing. Each layer was a square with a different edge length *a*, as shown in Table 4.

The corresponding height was measured and plotted in Fig. 11b. The layer thickness was obtained by applying a linear fit to the height of each layer of the square frustum. Based on the linear fitting result, 77 μm was the calibrated layer thickness, which will be used as the layer thickness in 3D printing. Note the fitted line does not pass through the origin. This is because the ink has different wettability on various substrates, i.e., when printing the first layer on the build platform and the subsequent layers on the previously printed layers.

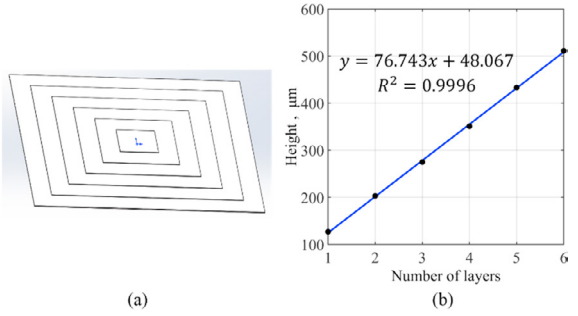

Fig. 11. Layer thickness testing. (a) CAD model used for layer thickness testing; and (b) linear fitting of the height on multi-layered square frustum.

5. Applications and Proof-of-concept for Multi-material Printing

To demonstrate the DDW's 3D printing ability and versatility, we designed and fabricated two 3D objects, as discussed in this section.

(1) Fig. 12Ac and 12Ad show a 3D USC Trojan logo (30 mm × 37 mm × 2.3 mm, 26 layers) printed on a piece of fabric using a self-solidifiable PU leather ink. A youtube video of the printing process can be found at [32]. The PU leather ink will solidify within 3 minutes at room temperature after its deposition. The rheological property of the ink is shown in Fig. 12Ag. The rheological behaviors were tested using a dial reading viscometer (Brookfield RVT, AMETEK. Inc.). The CAD model (See Fig. 12Aa) and the tool path of the printed 26 layers (See Fig. 12Ab) were generated using Autodesk ArtCAM Premium 2018. The corresponding parameter settings are listed in Table 7.

Note that, although the build platform used in this demo was a shoe fabric, which was not flat and had many small holes (around 50-100 μm), our DDW process can make sure the ink soak into the fiber and fill the gaps to generate a solid base for the following layers after printing the first layer. Simultaneously, the DDW process will not be affected by the needle's collision with the fabric surface. In comparison, such a collision issue would be a disaster for other DIW methods. Fig. 12Ae and 12Af show the details of some sharp edges of the printed part. The DDW process enables various types of inks and can be beneficial for applications such as wearable electronics and 3D printed shoes in the future.

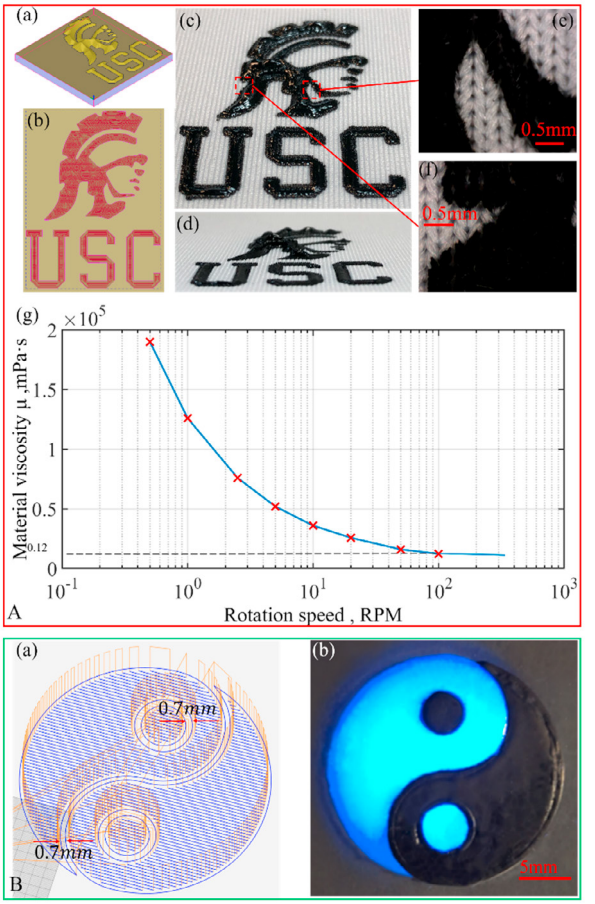

Fig. 12. Demo of 3D printing structures. (A) A USC Trojan logo printed on a piece of fabric. (a) CAD model; (b) tool path of the whole part (26 layers); (c)(d) the fabrication result; (e)(f) microscopic images showing the details; and (g) rheological property of the used PU leather ink. (B) Multi-layer stacked Tai Chi pattern printed using multiple materials. (a) The tool path of one layer; and (b) the fabrication result.

(2) Finally, to validate the multi-material 3D printing ability of the DDW process, we fabricated a multi-layer stacked Tai Chi pattern (23 mm × 2mm, 20 layers for the black portion and 25 layers for the white portion) using two printheads filled with two kinds of materials, respectively. This is like our previous work [34], but non-photocurable materials can be used here. As shown in Fig. 12Bb, the black part was printed using PU leather ink, and the white part was printed using photocurable TCP ink. The tool path of one layer is shown in Fig. 12Ba. For the designed pattern, the tool path was generated using Autodesk ArtCAM Premium 2018. The corresponding parameter settings are listed in Table 7. We achieved the same droplet diameter and line width for both inks by adjusting the dispensing gap. The difference in layer heights was compensated when printing different layers.

It can be observed that the boundary surface of the Tai Chi model is curved. This curved surface is common in the DIW and other droplet-based approaches. The curvature is governed by the capillary forces acting on the triple line defined by air,

solid platform, and liquid ink. As described by Young's relation,

$$\gamma_{LG}\cos\theta_E = \gamma_{SG} - \gamma_{SL} \quad (10)$$

Where γ are the interface tensions between the three phases (solid/liquid/gas), and θ_E is the equilibrium contact angle. This kind of curved surface due to partial wetting will affect printing the next layers and ultimately leading to fillet edges and expanded boundaries, as shown in Fig. 12Bb. Therefore, each component's boundary defined in the Tai Chi pattern was offset by 0.35 mm in both directions (See Fig. 12Ba, 0.7 mm boundary spacing in total) when building the pattern to avoid material contamination. The relationship between the part height and the expanded fillet edge should be considered when developing a tool path planning software for the DDW process in the future. Alternatively, additional supports can be added to the layer boundary to limit the expanded borders.

Table 7. Parameter settings for Trojan logo and Tai Chi pattern printing.

	PU leather ink	TCP ink
Motor rotation speed v_m (RPM)	960	960
Calculated punching speed v_p (mm/s)	160	160
Dispensing gap h_g (μm)	160	180
Corresponding droplet size D_d (μm)	~400	~400
X/Y-axis motion speed f (mm/s)	4.0	4.0
Calculated droplet spacing w_d (μm)	267	267
Corresponding line width w_l (μm)	~350	~350
Tool path spacing w_t (mm)	0.3	0.3
Layer height l_h (μm)	95	77
Bottom layer count for USC logo n_{bf}	2	
Total layer count for USC logo n_{USC}	26	
Bottom layer height on glass l_{hg} (μm)	151	125
Bottom layer count for Tai Chi n_{bg}	1	1
Total layer count for Tai Chi n_{TaiChi}	20	25

6. Conclusion and future work

A novel direct droplet writing process using the droplet-punching and capillary-splitting principles has been developed for highly viscous materials. The newly developed DDW-based 3D printing method has been demonstrated using liquid materials with viscosity as high as 190,000 mPa·s. In our design, a capillary tube driven by a servo motor is used to punch viscous materials out from the nozzle, and the punched-out material was then dispensed on the build platform through the liquid-bridge splitting mechanism. In addition to overcoming the material viscosity limitation, our contact-based DDW method also avoids common jetting issues caused by satellite droplets, droplet splashing, and deflection. In each dispensing cycle, only one single droplet will precisely and stably form at the position where the needle touches the substrate. We did a comprehensive process study and found the DDW process can achieve various droplet sizes by adjusting process parameters, including punching speed and dispensing gap. The positional accuracy will not be affected by printing speed and dispensing gap. Another advantage of DDW is its robustness. The material viscosity change will not affect the material printability and printing results for the same parameter settings. Finally, the results of several test cases have been presented to demonstrate the DDW process's effectiveness. Our work will drastically broaden the range of printable materials for the droplet-based 3D printing methods and significantly advance using such 3D printing methods in fabricating multi-material objects for various functional applications.

In the future, we would like to explore the tool path planning for the DDW process, including the curved boundary effect. We will also reduce the capillary tube size to investigate how to reduce the droplet size further. Besides the printing resolution, we will also increase the printing speed by using a DC servo motor with a higher rotational speed or involving reusable support for overhang features [35] or integrating DDW with the projection-based Stereolithography process [36]. Finally, we will investigate the use of multi-axis DDW process to print materials on any curved substrate. Therefore, the DDW method could provide a new direction in developing multi-material and multi-directional 3D printing methods in the future.

References

[1] Bijadi S, de Bruijn E, Tempelman EY, Oberdorf J. Application of Multi-Material 3D Printing for Improved Functionality and Modularity of Open Source Low-Cost Prosthetics: A Case Study. InFrontiers in Biomedical Devices 2017 Apr 10 (Vol. 40672, p. V001T10A003). American Society of Mechanical Engineers.

[2] Mohammed MI, Tatineni J, Cadd B, Peart G, Gibson I. Advanced auricular prosthesis development by 3D modelling and multi-material printing. InDesTech 2016: Proceedings of the International Conference on Design and Technology 2017 Jan 1 (pp. 37-43). Knowledge E.

[3] Macdonald E, Salas R, Espalin D, Perez M, Aguilera E, Muse D, Wicker RB. 3D printing for the rapid prototyping of structural electronics. IEEE access. 2014 Mar 13; 2:234-42.

[4] Liu Z, Zhang M, Bhandari B, Wang Y. 3D printing: Printing precision and application in food sector. Trends in Food Science & Technology. 2017 Nov 1; 69:83-94.

[5] Zhu M, Mori Y, Wakayama T, Wada A, Kawamura S. A fully multi-material three-dimensional printed soft gripper with variable stiffness for robust grasping. Soft robotics. 2019 Aug 1; 6(4):507-19.

[6] Zhu M, Xie M, Lu X, Okada S, Kawamura S. A soft robotic finger with self-powered triboelectric curvature sensor based on multi-material 3D printing. Nano Energy. 2020 Apr 17:104772.

[7] Vogt DM, Becker KP, Phillips BT, Graule MA, Rotjan RD, Shank TM, Cordes EE, Wood RJ, Gruber DF. Shipboard design and fabrication of custom 3D-printed soft robotic manipulators for the investigation of delicate deep-sea organisms. PloS one. 2018 Aug 1; 13(8):e0200386.

[8] Sun K, Wei TS, Ahn BY, Seo JY, Dillon SJ, Lewis JA. 3D printing of interdigitated Li-Ion microbattery architectures. Advanced Materials. 2013 Sep 6; 25(33):4539-43.

[9] Fu K, Wang Y, Yan C, Yao Y, Chen Y, Dai J, Lacey S, Wang Y, Wan J, Li T, Wang Z. Graphene oxide-based electrode inks for 3D-printed lithium-ion batteries. Advanced Materials. 2016 Apr; 28(13):2587-94.

[10] Brunton A, Arikan CA, Tanksale TM, Urban P. 3D printing spatially varying color and translucency. ACM Transactions on Graphics (TOG). 2018 Jul 30; 37(4):1-3.

[11] Morovič P, Morovič J, Tastl I, Gottwals M, Dispoto G. HANS3D: a multi-material, volumetric, voxel-by-voxel content processing pipeline for color and beyond. InColor and Imaging Conference 2017 Sep 11 (Vol. 2017, No. 25, pp. 219-225). Society for Imaging Science and Technology.

[12] Mirzaali MJ, Caracciolo A, Pahlavani H, Janbaz S, Vergani L, Zadpoor AA. Multi-material 3D printed mechanical metamaterials: Rational design of elastic properties through spatial distribution of hard and soft phases. Applied Physics Letters. 2018 Dec 10; 113(24):241903.

[13] Sundaram S, Skouras M, Kim DS, van den Heuvel L, Matusik W. Topology optimization and 3D printing of multimaterial magnetic actuators and displays. Science advances. 2019 Jul 1; 5(7):eaaw1160.

[14] Zhu B, Skouras M, Chen D, Matusik W. Two-scale topology optimization with microstructures. ACM Transactions on Graphics (TOG). 2017 Jul 25; 36(4):1.

[15] Ituarte IF, Boddeti N, Hassani V, Dunn ML, Rosen DW. Design and additive manufacture of functionally graded structures based on digital materials. Additive Manufacturing. 2019 Dec 1; 30:100839.

[16] Han D, Lee H. Recent advances in multi-material additive manufacturing: methods and applications. Current Opinion in Chemical Engineering. 2020 Jun 1; 28:158-66.

[17] Hon KK, Li L, Hutchings IM. Direct writing technology—Advances and developments. CIRP annals. 2008 Jan 1;57(2):601-20.

[18] Leung Y, Kwok T, Mao H, Chen Y. Digital material design using tensor-based error diffusion for additive manufacturing. Computer-aided Design. 2019; 114: 224-235.

[19] Kowsari K, Akbari S, Wang D, Fang NX, Ge Q. High-efficiency high-resolution multimaterial fabrication for digital light processing-based three-dimensional printing. 3D Printing and Additive Manufacturing. 2018 Sep 1; 5(3):185-93.

[20] Yang Y, Song X, Li X, Chen Z, Zhou C, Zhou Q, Chen Y, Recent progress in biomimetic additive manufacturing technology: from materials to functional structures. Advanced Materials. 2018, 30(36): 1706539.

[21] Leung Y, Kwok T, Li X, Yang Y, Wang CL, Chen Y, Challenges and status on design and computation for emerging additive manufacturing technologies. Journal of Computing and Information Science in Engineering. 2019; 19: 021013.

[22] Gruene M, Unger C, Koch L, Deiwick A, Chichkov B. Dispensing pico to nanolitre of a natural hydrogel by laser-assisted bioprinting. Biomedical engineering online. 2011 Dec 1; 10(1):19.

[23] Brown MS, Brasz CF, Ventikos Y, Arnold CB. Impulsively actuated jets from thin liquid films for high-resolution printing applications. Journal of Fluid Mechanics. 2012 Oct 25; 709:341.

[24] Zhang Z, Xiong R, Mei R, Huang Y, Chrisey DB. Time-resolved imaging study of jetting dynamics during laser printing of viscoelastic alginate solutions. Langmuir. 2015 Jun 16; 31(23):6447-56.

[25] Park JU, Hardy M, Kang SJ, Barton K, Adair K, kishore Mukhopadhyay D, Lee CY, Strano MS, Alleyne AG, Georgiadis JG, Ferreira PM. High-resolution electrohydrodynamic jet printing. Nature materials. 2007 Oct; 6(10):782-9.

[26] Galliker P, Schneider J, Eghlidi H, Kress S, Sandoghdar V, Poulikakos D. Direct printing of nanostructures by electrostatic autofocussing of ink nanodroplets. Nature communications. 2012 Jun 12; 3(1):1-9.

[27] Foresti D, Kroll KT, Amissah R, Sillani F, Homan KA, Poulikakos D, Lewis JA. Acoustophoretic printing. Science advances. 2018 Aug; 4(8):eaat1659.

[28] Yang Y, Gu S, Liu J, Tian H, Lv Q. Research and development of a 3D jet printer for high-viscosity molten liquids. Micromachines. 2018 Nov; 9(11):554.

[29] Lu S, Chen X, Zheng H, Zhao Y, Long Y. Simulation and experiment on droplet volume for the needle-type piezoelectric jetting dispenser. Micromachines. 2019 Sep; 10(9):623.

[30] Ledesma-Fernandez J, Tuck C, Hague R. High viscosity jetting of conductive and dielectric pastes for printed electronics. InProceedings of the International Solid Freeform Fabrication Symposium 2015 (pp. 40-55).

[31] Chen H, Tang T, Amirfazli A. Effects of surface wettability on fast liquid transfer. Physics of Fluids. 2015 Nov 3; 27(11):112102.

[32] Direct droplet writing demos: https://youtu.be/Orw-TsCaYW0.

[33] Li H, Yang Q, Li G, Li M, Wang S, Song Y. Splitting a droplet for femtoliter liquid patterns and single cell isolation. ACS applied materials & interfaces. 2015 May 6; 7(17):9060-5.

[34] Zhou C, Chen Y, Yang Z, Khoshnevis B. Digital material fabrication using mask-image-projection-based stereolithography. Rapid Prototyping Journal. 2013; 19(3): 153-165.

[35] Xu Y, Wang Z, Gong S, Chen Y. Reusable support for additive manufacturing. Additive Manufacturing. 2021 Mar 1;39:101840.

[36] Xu Y, Zhu Y, Sun Y, Jin J, Chen Y. A Vibration-Assisted Separation Method for Constrained-Surface-Based Stereolithography. Journal of Manufacturing Science and Engineering. 2021, 143(5), 051008.